MATERIALS SCIENCE

Internal ion-gated organic electrochemical transistor: A building block for integrated bioelectronics

George D. Spyropoulos[1]*, Jennifer N. Gelinas[2,3]†, Dion Khodagholy[1]*†

Real-time processing and manipulation of biological signals require bioelectronic devices with integrated components capable of signal amplification, processing, and stimulation. Transistors form the backbone of such circuits, but numerous criteria must be met for efficient and safe operation in biological environments. Here, we introduce an internal ion-gated organic electrochemical transistor (IGT) that uses contained mobile ions within the conducting polymer channel to permit both volumetric capacitance and shortened ionic transit time. The IGT has high transconductance, fast speed, and can be independently gated to create scalable conformable integrated circuits. We demonstrate the ability of the IGT to provide a miniaturized, comfortable interface with human skin using local amplification to record high-quality brain neurophysiological activity. The IGT is an effective transistor architecture for enabling integrated, real-time sensing and stimulation of signals from living organisms.

INTRODUCTION

Electronic systems that can acquire, process, and interact with biological substrates are increasingly used to understand dynamic living organisms and treat human disease. These responsive systems are critical for establishing causality in complex experimental paradigms (*1*, *2*) and have been shown to increase efficacy and tolerability of therapy for a range of disorders (*3*). Transistors are necessary components of these systems, forming the building blocks of circuits capable of performing specific operations such as signal amplification, filtering, detection of signal characteristics, and delivery of electrical or chemical stimulation. Key features required for safe, efficient, and prolonged use of transistors in biological environments include (i) biocompatibility and stability of constituent materials, (ii) substrate conformability to prevent mechanical mismatch with tissue, (iii) high speed and amplification to detect potentially low-amplitude signals at physiologically relevant time scales, and (iv) independent gating to enable integrated circuit computations.

Although a wide range of transistor architectures and materials are available, none incorporates all of these features. Conventional silicon-based field-effect transistors (FETs) can be fabricated into multielectrode arrays to acquire data from neural tissue in vitro and in vivo (*4*, *5*), but the large mechanical mismatch between Si and the tissue, as well as its lack of biocompatibility, precludes chronic use in humans because of risk of neural damage. Flexibility can be enhanced by combining small prefabricated thinned Si parts onto plastic substrates (*6*, *7*). Alternatively, organic materials can be used as semiconducting channels to create organic FETs (OFETs), which are intrinsically flexible and compatible with the low-temperature processing required for fabrication on ultrathin plastic substrates (*8*–*11*). However, FETs are susceptible to damage by water or ion penetration and need to be fully encapsulated for use in physiologic environments (*12*), introducing bulk and decreasing performance. To overcome these limitations and increase the efficiency of ion-to-electron conversion, electrolyte-gated OFETs (EGOFETs) were developed (*13*–*21*). EGOFET architecture allows the transistor channel to come into direct contact with the electrolyte and form an electric double-layer capacitance between the transistor channel's surface and ions of electrolyte. Elimination of the gate dielectric between the channel and electrolyte improves EGOFET capacitance compared to conventional FETs. Yet, this structural reduction also impedes independent gating ability because ions in the electrolyte are required for operation and are shared between all transistors in a device. Therefore, it is not possible to create integrated bioelectronic circuits with EGOFETs.

FETs transduce signals through a double-layer capacitance formed at the semiconductor's surface, restricting the area available for ion-to-electron conversion. In contrast to FETs, organic electrochemical transistors (OECTs) permit movement of ions into and out of the hydrophilic conducting polymer-based channel, resulting in volumetric capacitance (*22*–*24*). OECTs can achieve high transconductance and reliably interface with a variety of biological substrates, including plants (*25*), the blood-brain barrier (*26*), metabolites (*27*), cell cultures (*28*), and neural tissue (*29*), as well as neuromorphic devices (*30*, *31*). Although OECTs are efficient transducers, they cannot be used as components of bioelectronic circuits because, similar to EGOFETs, the electrolyte is an integral part of the transistor and cannot provide individualized input to specific transistors. In addition, the speed of OECTs is defined by the time taken for ions to travel between the electrolyte and polymeric channel (*32*). Although channel geometry can be miniaturized using microfabrication techniques (*33*), device operation speed remains inadequate for use in responsive bioelectronic systems.

Here, we introduce a biocompatible, conformable, stable, high-speed, high-transconductance transistor architecture to enable integrated bioelectronics. These internal ion-gated organic electrochemical transistors (IGTs) have mobile ions embedded in the conducting polymer of the transistor channel, creating a self-(de)doping process that eliminates the need for ion exchange from a shared external electrolyte. This characteristic permits both individualized transistor gating and a time constant of 2.6 μs, substantially faster than electrolyte-based transistors. We combined IGTs to create conformable integrated circuits, including digital logic gates and cascaded amplifiers. We validated IGT performance by microfabricating devices that could be conformally adhered between human hairs on the scalp without chemical adhesives and recorded physiologically

[1]Department of Electrical Engineering, Columbia University, New York, NY 10027, USA. [2]Department of Neurology, Columbia University Medical Center, New York, NY 10032, USA. [3]Institute for Genomic Medicine, Columbia University Medical Center, 630 West 168th Street, New York, NY 10032, USA.
*These authors contributed equally to this work.
†Corresponding author. Email: jng2146@cumc.columbia.edu (J.N.G.); dion@ee.columbia.edu (D.K.)

relevant electroencephalography (EEG) signals suitable for advanced data processing.

RESULTS

The channel of the IGT was composed of the conducting polymer poly(3,4-ethylenedioxythiophene) polystyrene sulfonate (PEDOT:PSS) combined with D-sorbitol. PEDOT:PSS is biocompatible, stable, and highly conductive, ensuring efficient ion-to-electron conversion. D-sorbitol is a biocompatible hydrophilic sugar alcohol that uptakes water molecules. We hypothesized that combining these materials would maintain a supply of ions within the conducting polymer, creating an "ion reservoir" and facilitating ion movement within the channel. Addition of D-sorbitol also improves the conductivity of PEDOT:PSS by enhancing the elongation of PEDOT-rich domains, an effect that is similarly observed with addition of solvents such as ethylene glycol (*34*–*36*). The transistor architecture was realized by forming channels, each with independent ion reservoirs, between two Au-based source and drain electrodes (Fig. 1A and fig. S1). To allow independent gating of individual transistors, the gate electrode must have efficient ionic, but not electronic, conduction with the bulk of the channel. Therefore, we introduced chitosan as an ion membrane between the gate and channel. Chitosan was chosen for this purpose because of its biocompatibility, stability, and solution processability (*37*, *38*). To reduce the electrochemical impedance between the Au gate electrode and chitosan ion membrane, we deposited a layer of PEDOT:PSS directly onto the Au (figs. S2 and S3). The overall device architecture was created using established microfabrication processes, verified by cross-sectional electron microscopy, and resulted in high-yield, reliable devices (Fig. 1B). This IGT operated in depletion mode, such that when a positive gate voltage was applied, mobile ions within the ion reservoir that were in the vicinity of PEDOT-rich regions of the film compensated the sulfonate anions on the PSS. This process led to a decrease of the hole density in the PEDOT and, consequently, a decrease in the channel current. The reaction was reversed upon applying a negative gate voltage (Fig. 1C). Because of the material process employed, the predominant source of the mobile ions was the mixture of ions present in the PEDOT:PSS dispersion. We elucidated the effect of varying the ion species on device performance by first deionizing the PEDOT:PSS film and then introducing specific salts (NaCl, KCl, $MgCl_2$, and $CaCl_2$). Ions with large hydrated radii (Mg^{2+} and Ca^{2+}) exhibited the slowest modulation. The monovalent ions with smaller hydrated radii (Na^+ and K^+) had faster time constants (fig. S4, A and B). The substantial changes in the time constant and modulation magnitude of the drain current due to altering the mobile ion species present support the direct involvement of these ions in the dedoping of the channel and suggest that monovalent ions enable the smallest relative time constant.

IGTs could be geometrically designed to maximize transconductance (32.30 mS) and performed comparably to other OECTs with substantially larger and nonpolarizable gates (Fig. 1D). It is important to note that there is no barrier to prevent the exit of ions into the ion membrane of the IGT, although appropriate biasing and application of gate potential effectively prevent this from occurring during normal device operation. Therefore, it is possible to dope and dedope the conducting polymer repetitively without a decrement in speed or significant drift in drain current (fig. S5A) while maintaining an equal rise time for doping and dedoping (Fig. 2, A and C). To highlight the IGT operating mechanism, we created an experiment

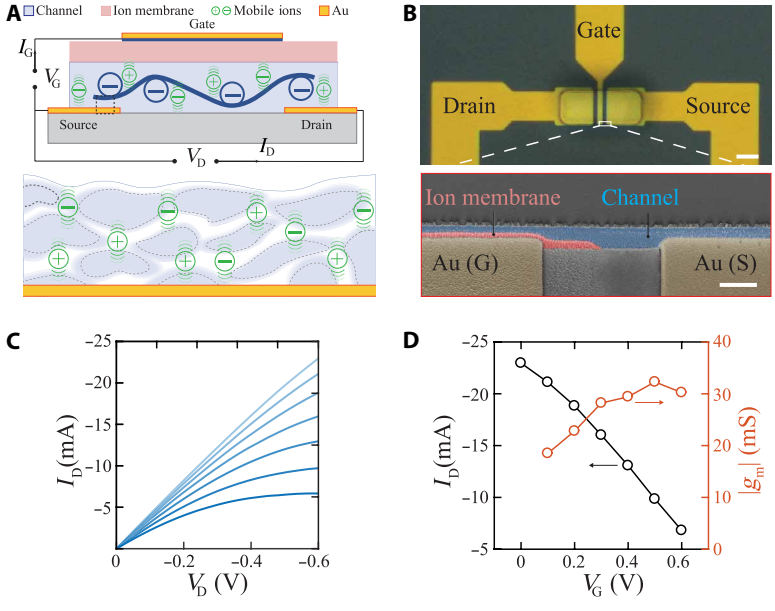

Fig. 1. Structure and steady-state characteristics of IGT. (**A**) Schematic illustration of IGT cross section and wiring diagram for device operation (top). D-sorbitol creates an ion reservoir, maintaining mobile ions (green) that can travel within the channel; PEDOT-rich regions are shown in light blue and PSS lamellas in white (bottom). (**B**) Optical micrograph displaying the top view of an individual transistor. Scale bar, 20 μm. Inset shows a cross-sectional scanning electron microscopy (SEM) image acquired at a tilt angle of 30°. Ion membrane (light red), channel (light blue), and Au contacts for gate (G) and source (S; beige) are visible. Scale bar, 5 μm. Note that PEDOT:PSS coating of gate electrode is not visible in the image. (**C**) Output characteristics ($I_D - V_D$) of IGT device ($L = 5$ μm, $W = 500$ μm) for gate voltage (V_G) varying from 0 V (top curve) to +0.6 V (bottom curve) with a step of +0.1 V; color intensity corresponds to V_G amplitude. (**D**) Transfer curve for $V_D = -0.6$ V (black), and the corresponding transconductance (orange), $|g_m max| = 32.30$ mS.

using high gate voltage stress, capable of forcing the ions to exit the channel and enter the ion membrane. These parameters resulted in different time constants for doping and dedoping, causing an asymmetrical drain current response (Fig. 2, B and D). This experiment supports the notion that the mobile ions can be maintained in the channel and are critical for the fast (de)doping of the conducting polymer.

Because the mobile ions in the channel were distributed throughout the conducting polymer, the (de)doping process involved the entire channel thickness, resulting in volumetric capacitance. Consequently, IGT transconductance increased with channel thickness (Fig. 2E). We developed an array of IGTs that geometrically varied in channel length and width over two orders of magnitude (5 to 500 μm; fig. S1). The transconductance of IGTs increased proportionally with respect to both the channel thickness and volume (Fig. 2F). A similar volume-based relationship was observed for the IGT I_{On}/I_{Off}, with a maximum value of ~4×10^6 (fig. S6).

We hypothesized that the existence of local mobile ions within the channel of the IGT would decrease the distance that ions are required to travel in order to participate in the (de)doping process, increasing the speed of the device relative to a conventional OECT, where ions are located in an external electrolyte. To test this assertion, we fabricated devices that could directly compare IGT and conventional OECT architectures. The IGT and OECT had identical geometry, with the OECT using a Ag/AgCl gate electrode immersed in electrolyte to minimize gate voltage drop at the gate electrode–electrolyte interface (Fig. 3A). These devices had similar transconductances (g_m = 0.8 mS; fig. S7), but the rise time of the IGT was significantly faster than that of the OECT (31.7 μs versus 191.2 μs; Fig. 3B). Next, we sought to confirm that the boost in IGT rise time was attributable to mobile ions within the channel, rather than (i) the longer distance between the gate and channel in the OECT or (ii) the ionic conduction of the chitosan membrane substituting for electrolyte, causing the device to operate akin to a solid-state OECT (*39*). We therefore fabricated devices that were identical apart from the presence of D-sorbitol combined with PEDOT:PSS (Fig. 3C). The speed of the device with IGT architecture (mobile ions within the channel) again surpassed that of the solid-state OECT, even when the solid-state OECT was operated under hydrated conditions (46 ms versus 1.82 s; Fig. 3D and corresponding output and transfer curves in fig. S8).

We then investigated whether embedded mobile ions located within the conducting polymer (in the ion reservoir) were sufficient to dedope the channel. To prevent any contribution of ions from

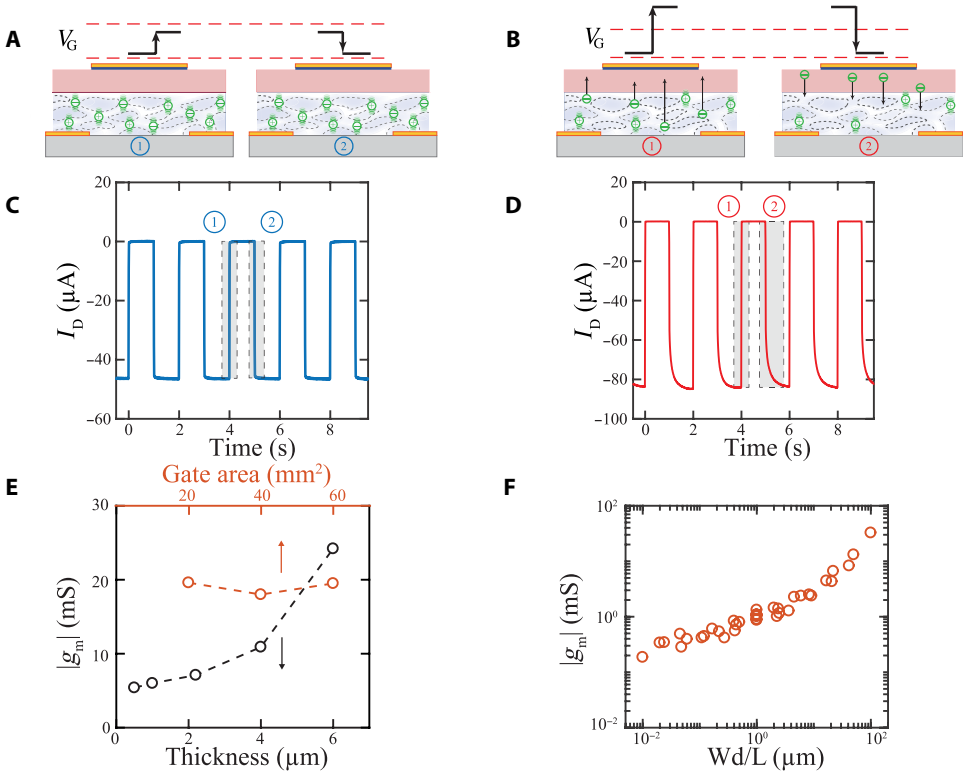

Fig. 2. Internal mobile ions enable volume-based, fast, symmetric, and repetitive (de)doping of the conducting polymer channel. (**A**) Schematic cross-sectional illustration of IGT under normal operating conditions, with mobile ions maintained in the ion reservoir of the channel. (**B**) Schematic cross-sectional illustration of IGT at high gate voltage stress capable of forcing the ions to exit the channel and enter the ion membrane. Dashed red lines represent lower and upper bounds of V_G during normal device operation. (**C**) Temporal response of the drain current (I_D) highlighting a symmetrical rise (dedoping; gray boxed area 1) and fall (doping; gray boxed area 2) time of the drain current in response to pulsed gate voltage [V_{DS} = −0.4, V_{GS} pulse amplitude = 0.4 V (note that the device is turned off); bottom, L = 5 mm, W = 10 mm]. (**D**) Asymmetrical temporal response of the drain current (longer doping time; gray boxed area 2 compared to dedoping time in gray boxed area 1) resulting from longer ion transit distance [(V_{DS} = −0.4, V_{GS} pulse amplitude = 0.9 V; bottom, same device as (C)]. (**E**) Maximum transconductance of an IGT as a function of channel thickness (black) and gate area (orange); channel L = 5 mm, W = 10 mm. Transconductance was calculated from a transfer curve for V_D = −0.6 V. (**F**) Maximum transconductance as a function of channel geometry. Transconductance was calculated for a 6 × 6 array of IGTs with logarithmically increasing channel length and width (fig. S1C) from a transfer curve for V_D = −0.6 V.

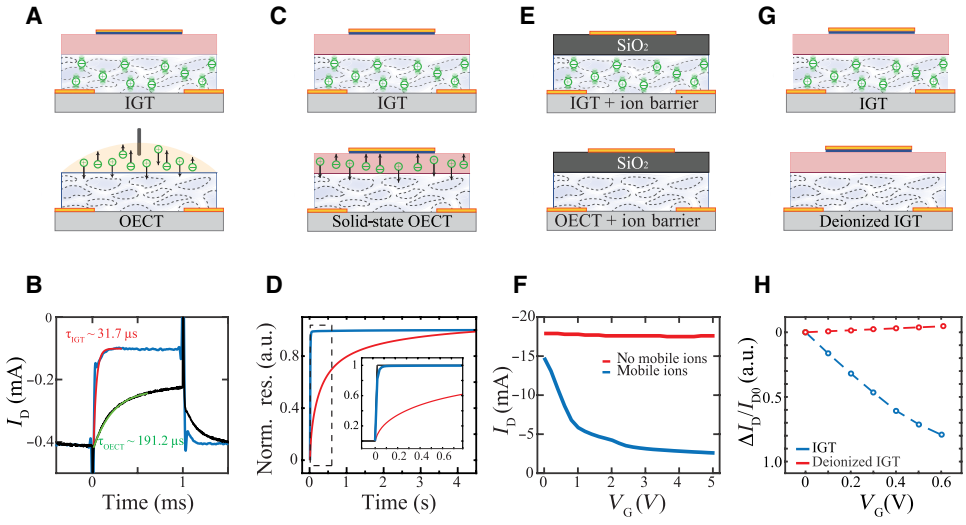

Fig. 3. Contained mobile ions within the channel are necessary and sufficient for IGT operation. (**A**) Schematic cross-sectional illustration of IGT with contained mobile ions (top) versus OECT with external electrolyte (bottom). The IGT channel acts as ion reservoir, maintaining mobile ions in the vicinity of PSS anions, allowing faster (de)doping processes, whereas the OECT depends on diffusion of ions from an electrolyte into the channel. Note that the channels of both transistors contained sorbitol. (**B**) Temporal response of the drain current (I_D) of an IGT (blue) and OECT (black) with the same dimension of channel ($L = 30$ μm, $W = 12$ μm, V_{GS} pulse amplitude = 0.3 V). Exponential fit of the IGT drain current (red), resulting in a time constant of 31.7 μs, and of the OECT drain current (green), resulting in a time constant of 191.2 μs. (**C**) Schematic cross-sectional illustration of IGT with contained mobile ions (top) versus solid-state OECT with ions in a solid-state electrolyte layer (lower). (**D**) Normalized temporal response of the I_D of an IGT (blue) versus the solid-state OECT (red) with the same dimension of channel ($L = 5$ mm, $W = 10$ mm); V_G is shown in black. Inset magnifies the region of the response enclosed by the black dashed lines. IGT had a faster time response ($\tau_{IGT} = 46$ ms) compared to the solid-state OECT ($\tau_{OECT} = 1.82$ s). (**E**) Schematic cross-sectional illustration of a PEDOT:PSS (no mobile ions; top) and PEDOT:PSS + D-sorbitol (with mobile ions; bottom) channel devices, both with a SiO_2 ion barrier layer. (**F**) Transfer curve for $V_D = -10$ V of a PEDOT:PSS (red) versus PEDOT:PSS + D-sorbitol (blue) channel gated through a 90-nm-thick SiO_2 layer; only the PEDOT:PSS + D-sorbitol device demonstrated modulation [same device geometry as (D)]. (**G**) Schematic cross-sectional illustration of IGT with contained mobile ions (top) versus deionized IGT (mobile ions removed from the channel; bottom). (**H**) Normalized transfer curve for $V_D = -0.5$ V of the IGT with deionized channel (red) versus normal IGT (blue). a.u., arbitrary units.

external sources, we replaced the chitosan ion membrane with a silicon dioxide ion barrier layer (thickness d = 90 nm) that enables only capacitive coupling between the gate and channel. Silicon dioxide was selected for this purpose because it prevents ion conduction, even at high voltages. The channel area was defined between two Au-based source and drain electrodes deposited on the SiO_2 layer, and gate voltage was applied through the bulk Si using a Au contact. We compared the modulation of channel current with respect to gate voltage between a channel composed of only PEDOT:PSS and a channel with PEDOT:PSS plus D-sorbitol to introduce embedded mobile ions (Fig. 3, E and F; red and blue traces, respectively). Only the channel with embedded mobile ions demonstrated modulation, confirming the ability of these channel-contained ions to dedope the conducting polymer. Last, to demonstrate that mobile ions in the reservoir are the primary ionic charge carriers involved in IGT operation, we compared a regular IGT with one that had a deionized channel (Fig. 3G). The deionized channel showed no modulation (Fig. 3H), confirming the inability of intrinsic charges of PEDOT:PSS and/or ion membrane (such as protons) to dedope the conducting polymer. We deionized the channel by repetitive soaking in DI water, a process that did not damage the device, as subsequent reintroduction of ions allowed recovery of drain current modulation (fig. S4, A and B). We additionally verified these results by using ion membranes that are not intrinsically proton conductors (such as gelatin and agar) in the fabrication of the IGT, revealing similar modulation to an IGT with a chitosan ion membrane (fig. S4C). Together, these results establish that embedding mobile ions in the IGT channel is a necessary element for the high transconductance and speed of the device.

To explore the limits of IGT speed, we fabricated progressively smaller IGTs and observed a time constant of 2.6 μs with 12 μm by 5 μm channel area (Fig. 4, A and B). This time constant translates into an effective bandwidth of 380 KHz, several orders of magnitude faster than previously reported electrolyte-gated transistors, including those with smaller channel dimensions (*21*, *24*, *40*).

Because IGTs have high performance (speed and transconductance), capacity for independent gating and are amenable to simple, scalable fabrication, they constitute an optimal building block for integrated bioelectronics. They also maintain stable operation over extended time periods (100 days; fig. S5). Although it is theoretically possible to develop integrated circuits using solid-state electrolyte-gated devices, speed is restricted by the ion exchange time between the electrolyte and the channel, and difficulties in patterning the electrolyte limits the minimal device geometry (*23*, *39*, *41*–*43*). We fabricated conformable IGT-based NAND and NOR digital logic gates on 2-μm-thick parylene-C supports (Fig. 5A). These logic gates accurately performed the corresponding arithmetic (Fig. 5B), confirming the scalability of IGT architecture for use as bioelectronic computational modules. Physiologic signal acquisition typically requires multistage amplification to ensure appropriate gain and enable between-stage processing (e.g., filtering and rectification). Therefore, we designed cascaded IGTs (Fig. 5C),

capable of multistage amplification and higher overall gain than a single transistor. The first IGT (T1) registered the input from its gate electrode and amplified it. The output current from T1 was converted to voltage using a resistor and then connected to the gate of the second-stage transistor (T2). We tested the amplification process by inputting a 25-mV-amplitude sine wave to the cascaded IGTs and observed a fourfold increase in amplification compared to a single transistor (Fig. 5D). The resistor value controlled the amplification of the circuit, with higher values resulting in increased gain, but at the cost of increased output impedance. We opted for a relatively low resistor value (100 ohms) because lower output impedance facilitates downstream processing, such as signal filtering or analog to digital conversion. We therefore demonstrated the ability of IGTs to form conformable integrated circuits and implement operations not possible with single-device strategies.

The established features of IGTs render them highly suitable for application to human EEG, and we selected this platform to demonstrate translational capacity of the device. Current clinical EEG uses rigid metal electrodes that require strong chemical adhesives to bond to the scalp. These electrodes must be relatively large (0.5 to 1 cm) and often interface with the skin through an additional layer of ionic conducting gel to attain sufficiently low electrochemical impedance to record neural activity. We hypothesized that the introduction of IGTs for EEG would (i) improve participant comfort by eliminating the need for adhesive and rigid materials affixed to the scalp, (ii) decrease the necessary electrode size, and (iii) ensure high signal-to-noise acquisition within physiological frequency bands.

We first compared the placement process between IGTs and conventional clinical electrodes. A Ag/AgCl cup electrode was affixed to the forehead of a human participant using collodion, which is routinely used for prolonged clinical EEG recordings, and ionic conducting gel was injected to serve as the interface. We fabricated two IGTs into a conformable ribbon structure (μ-EEG IGT) and placed it on the opposite side of the participant's forehead. The μ-EEG IGT adhered directly to the skin without use of additional chemicals because of

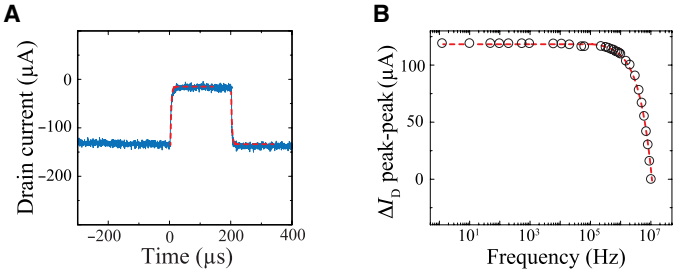

Fig. 4. Contained mobile ions enable high-speed and wide-bandwidth IGTs. (**A**) Temporal response of the drain current (I_D) of an IGT device with $L = 12$ μm and $W = 5$ μm. Exponential fit of the IGT drain current (red), resulting in a time constant of 2.6 μs ($n = 512$). (**B**) Small-signal peak-to-peak drain current ($I_{D\text{-}PP}$) of an IGT operating at $V_D = -0.6$ V and $V_G = 100$ mV peak-to-peak sine wave, resulting in 380 kHz of effective bandwidth ($\Delta I_{P\text{-}P}$ was composed of the average of 10 cycles for each frequency).

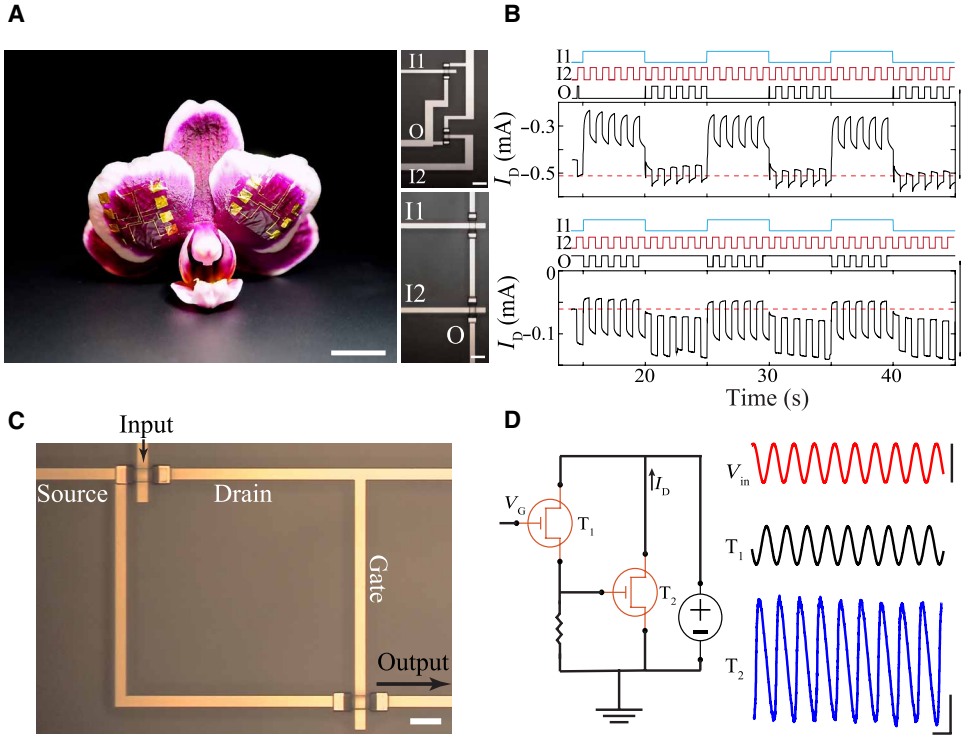

Fig. 5. Integrated IGT-based digital logic gates and cascaded amplifiers. (**A**) IGT-based NAND and NOR gates conform to the surface of orchid petals (left). Scale bar, 1 cm. Optical micrographs of NOR (top right) and NAND (bottom right) logic gates. Input (I1 and I2) and output (O) configuration is indicated. Scale bar, 100 μm. (**B**) Temporal response of the output (O) drain current of a NOR (top) and a NAND (bottom) logic gate. First input signal (I1, blue), second input signal (I2, red), and output signal (O, black) are shown at the top. Dashed red lines mark the threshold of high and low logics. (**C**) Optical micrograph displaying the top view of an IGT-based cascaded amplifier. Scale bar, 20 μm. (**D**) Circuit diagram of IGT-based cascaded amplifier and the corresponding input and output signals. Input voltage, V_{in}, (red). Scale bar, 50 mV. Output signal from T1 (black). Final amplified output from T2 (blue). Scale bars, 50 μA and 100 ms. (Photo credit: Jennifer Gelinas, Columbia University)

its lightweight and conformable structure that requires minimal force to maintain contact (Fig. 6A, top). Sorbitol can also be used as a gate electrode coating to serve as an intrinsic adhesive to the scalp (*36*). The clinical electrode and μ-EEG IGT were kept on the forehead for 1 hour and then removed. No skin redness or irritation was visible in the area where the μ-EEG IGT had been placed, in clear contrast to the region where the clinical electrode was located (Fig. 6A, bottom).

Next, we addressed electrode placement in areas of the scalp covered by hair, which is of key importance since the majority of the standardized EEG electrode placements are located in these areas. Clinical EEG electrodes are affixed over multiple hair follicles, increasing impedance across the electrode-scalp interface (*44*). Two 50 μm by 100 μm μ-EEG IGT channels were fabricated into a 1.5-mm-wide ribbon. These dimensions ensured that the entire device conformed to the scalp in between hair follicles but could also be easily manually manipulated, thereby improving mechanical and electrical stability (Fig. 6B).

To test the ability of the μ-EEG IGT to acquire high-quality neurophysiological signals, we placed it over the left occipital region (O1; based on International 10-20 system of EEG electrode placement) and recorded relative to a reference electrode over the left forehead (Fp1). With this recording configuration, we aimed to capture the posterior dominant rhythm, an 8- to 12-Hz (α) oscillation that occurs over the occipital region during quiet wakefulness with eyes closed. The human participant self-identified epochs of eye closure using a switch synchronized to the EEG recording. A 500-ohm resistor placed in series with the IGT channel converted current to voltage, and this output was recorded using an Intan acquisition system (Fig. 6C). The lower limit of the bandwidth was set at 0.1 Hz to eliminate amplifier saturation due to the IGT baseline voltage. The μ-EEG IGT acquired clear neurophysiological signal, as confirmed by the consistent appearance of ~10-Hz activity over the occipital region with eye closure, in keeping with a posterior dominant rhythm (Fig. 6D). The spectrogram of the neural signal also revealed higher-frequency activity coupled to appearance of the posterior dominant rhythm. As the co-occurrence of brain oscillations with different frequencies has been linked to various neural computations and information transfer between cortical areas (*45*, *46*), we further investigated these higher frequencies. Cross-frequency coupling analysis revealed a significant coupling between α and β (13 to 25 Hz) frequency bands, as well as between β and low γ (30 to 50 Hz), highlighting the ability of the μ-EEG IGT to acquire a range of physiologically relevant frequencies and generate data suitable for system-level analysis (Fig. 6E; $P < 0.05$ with Bonferroni correction).

DISCUSSION

We developed a novel organic electrochemical transistor architecture, the IGT, that operates via mobile ions embedded within a polymeric channel. We used D-sorbitol to maintain an ion reservoir within the PEDOT:PSS and demonstrated that these local mobile ions are necessary and sufficient to dedope the conducting polymer without an external ionic source. These ions are distributed throughout the conducting polymer in the channel, enabling volumetric capacitance and resulting in high transconductance. By reducing the distance that ions are required to travel to participate in the (de) doping process, IGTs have a significantly faster time response compared to electrolyte-driven transistors that have equal or smaller geometries. IGTs also have independent gates, making it possible to use them as components of integrated circuits. We used IGTs to create conformable digital logic gates and cascaded amplifiers. The

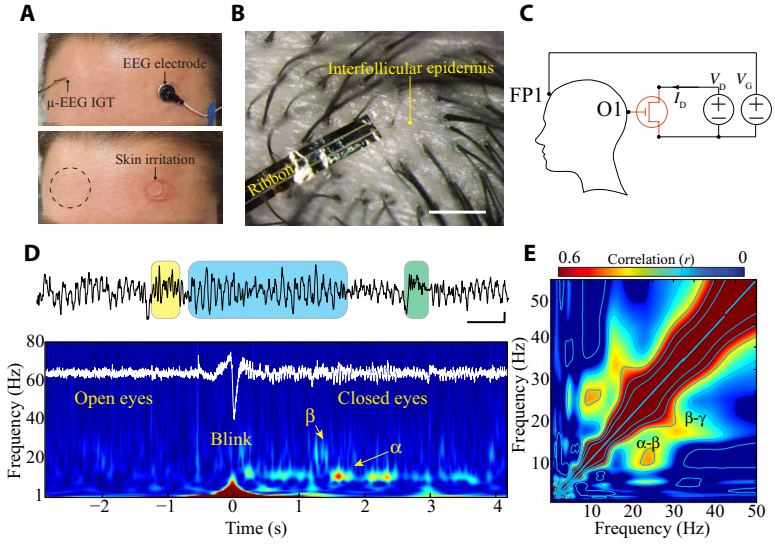

Fig. 6. Micrometer-scale IGTs acquire high-quality human EEG signals. (**A**) Photograph of μ-EEG IGT (top left) and clinical EEG electrode (top right) mounted on the forehead of a healthy volunteer. Corresponding photograph after μ-EEG IGT and clinical EEG electrode were removed 1 hour later (bottom left and right); skin irritation was visible only in the vicinity of the clinical EEG electrode. (**B**) Optical micrograph of μ-EEG IGT conforming to human scalp; devices were designed to fit the interfollicular epidermis. Scale bar, 2 mm. (**C**) Wiring diagram of EEG recording using a μ-EEG IGT at $V_D = -0.6$ V and $V_G = 0.4$ V. Left frontopolar (FP1) and occipital (O1) regions were used for device placement. (**D**) Sample time trace of the signal recorded from O1 with μ-EEG IGT demonstrating alpha (α, blue), beta (β, yellow), and low gamma (γ_{low}, green) oscillations (top). Time-frequency spectrogram of μ-EEG IGT recording demonstrating reactivity of posterior dominant rhythm to eye closure. Eye blink artifact is visible. Scale bar, 500 ms, 100 μV. Warmer colors represent higher relative power in in arbitrary units. (**E**) Comodulogram showing the cross-frequency coupling of the same recording epoch; significant coupling between α-β and β-γ_{low} is indicated. (Photo credit: George Spyropoulos, Columbia University)

combination of high transconductance, high speed, and independent gating permits IGTs to perform operations not currently possible with electrolyte-driven transistors.

IGTs are composed of only biocompatible and commercially available materials that can be processed using established microfabrication techniques (*24*). These materials do not require encapsulation in a biological environment because they are not toxic, and furthermore, the operation of the IGT is not impaired by exposure to water or ions. IGTs are also intrinsically flexible as their main constituents are polymers and polysaccharides. Because IGT fabrication needs only low-temperature processes, it is compatible with integration into a wide variety of conformable plastic substrates. Therefore, IGTs constitute an optimal solution for implantable integrated bioelectronic circuits.

We demonstrated how IGT-based devices could benefit human EEG, a critical clinical and research procedure. The μ-EEG IGT acquired high-quality neurophysiological data from a human participant. No chemical adhesives were required, leading to the absence of skin irritation and improved comfort. IGT local amplification directly at the device-scalp interface permitted contact size to be decreased by five orders of magnitude, and the device easily fit between hair follicles, substantially simplifying placement. In addition to serving as miniaturized transducers, IGTs have the capacity to process and interact with biological signals by forming integrated closed loop systems. The unique features of IGT-based devices facilitate potential applicability to a broad range of bioelectronics that require safe, chronic implantation in humans, including brain-machine interfaces, wearable electronics, and therapeutic responsive stimulation devices.

MATERIALS AND METHODS

IGT fabrication

PEDOT:PSS (Clevios PH1000) was acquired from Heraeus. D-sorbitol (≥99.5%; BioUltra), chitosan (low molecular weight), (3-glycidyloxypropyl)trimethoxysilane (GOPS), 4-dodecyl benzene sulfonic acid (DBSA), 3-(trimethoxysilyl)propyl methacrylate (A-174 silane), and Micro 90 concentrated cleaning solution were purchased from Sigma-Aldrich. The 495 PMMA A4 (polymethyl methacrylate) resist was purchased from MicroChem. AZnLOF2020 (negative photoresist), AZ9260 (positive photoresist), AZ 400 K, and AZ 726 MIF (metal ion free) developers were acquired from MicroChemicals, Merck.

Cleaned 100-mm quartz wafers (thickness of 1 mm) were coated with a 2-μm-thick parylene layer, which provided a conformable substrate. We patterned the Au electrodes and interconnects via photolithography and lift-off processes. AZnLOF2020 was spin-coated (3000 rpm), baked on a proximity hot plate at 110°C for 90 s, exposed using a Suss MA6 Mask Aligner, and developed with AZ 726 MIF developer. Ti (10 nm) and Au (100 nm) layers were deposited with an e-beam metal evaporator (CHA Mark 50). Lift-off was performed by immersing the substrates in a bath with a 1165 stripper. An additional 2-μm parylene layer was coated on the samples to electrically isolate the Au electrodes. The adhesion of the second parylene layer was improved by using 3-(trimethoxysilyl)propyl methacrylate (A-174 silane) during coating. We spin-coated a dilution of micro 90 (8% in DI water) to form an antiadhesive layer. A sacrificial third parylene layer (2 μm) was deposited on top. We etched the areas that corresponded to transistor channels and contact pads via successive photolithography and plasma etching steps. AZ9260 was spin-coated (5000 rpm), baked at 115°C for 90 s, exposed using a Suss MA6 Mask Aligner, and developed with AZ400K developer (1:4 with DI water). The patterned areas were etched with a plasma reactive ion etching process [Oxford Plasmalab 80; 180 W, 50-sccm (standard cubic centimeters per minute) O_2, and 2-sccm SF_6]. A ~200-nm PEDOT:PSS (1% GOPS) and a ~700-nm chitosan (without any additional salt) layer were spin-coated successively to form the ion membrane interface that covers the gate electrode. To pattern the ion membrane, we used, in a similar manner to previous steps, photolithography and plasma etching after depositing a thin, protective PMMA layer (~200 nm) (*37*). Rinsing with acetone removed the photoresist and PMMA residues, leaving the ion membrane layers intact. Last, to realize the transistor channels, we spin-coated a mixture of PEDOT:PSS with D-sorbitol [40% D-sorbitol, 1% GOPS (as a cross-linker), and 0.1% DBSA (to improve film processing and wettability)] and patterned it by peeling off the third parylene layer (fig. S1). Unless otherwise stated, all films were deposited at 3000 rpm, resulting in approximately 2-μm-thick films. Care was taken to ensure complete coverage of metal pads by the conducting polymer to minimize parasitic capacitances. For deionized channel experiments, PEDOT:PSS films with the cross-linker (GOPS) were repetitively soaked in DI water baths five times, followed by deposition (spin coating at 1000 rpm) of 100% (w/v) sorbitol in DI water. To reintroduce ions into these devices, the DI water was replaced by a salt solution [phosphate buffered saline (PBS), NaCl, KCl, $CaCl_2$, or $MgCl_2$].

Electrical characterization

Current-voltage characteristics were measured with a Keysight B2902A Precision Source/Measurement Unit using two channels. On the first channel (V_D), linear sweeps from 0 V to −0.6 V with a step of −0.03 V were applied. On the second channel (V_G), constant voltages from 0 to 0.6 V or 1.2 V were applied. The electrical characteristics of OECTs were measured with 1× PBS as an electrolyte and Ag/AgCl as gate electrodes. Temporal responses for IGTs, IGT-based logic gates, and OECTs were recorded with a Keysight InfiniiVision DSOX2002A digital storage oscilloscope under pulse excitation from a Keysight 33500B Series waveform generator and applied constant V_D from a Keysight B2902A. We derived the drain current by measuring the voltage drop across a 100-ohm series resistor with the IGT channel. Time constant was extracted by fitting the rise time of the drain current with a single exponential decay equation. Electrochemical impedance spectroscopy was performed with a Gamry Instruments Reference 600^+ using a three-electrode configuration with platinum and Ag/AgCl as counter and reference electrodes, respectively.

Photolithography and plasma etching steps were used to prepare cross sections of the IGTs. We acquired scanning electron microscopy (SEM) images of those cross sections with a Zeiss Sigma VP scanning electron microscope. Before imaging the devices, a ~10-nm AuPd layer was sputtered. The SEM images were taken with an acceleration voltage of 1.5 kV at a tilt angle of 30°.

EEG recordings

All EEG recordings were performed on a healthy volunteer. PEDOT:PSS-coated Au electrodes were placed on the scalp of the volunteer on left frontopolar (FP1) and occipital (O1) positions. The gate (G) and source (S) of the IGT were connected to O1 and FP1 positions, respectively. During EEG recording, IGT operated at V_D = −0.6 V

and V_G = 0.4 V. EEG signals were acquired at a sampling rate of 1 kHz with a band-pass filter of 0.1 to 500 Hz, using a custom board containing an RHD2164 die (Intan Technologies) and visualized in real time using RHD2000 Interface Software (Intan Technologies). The drain current was determined by measuring the voltage drop across a 500-ohm series resistor. Data were stored for off-line analysis with a 16-bit format, analyzed using MATLAB (MathWorks), and visualized using NeuroScope (neurosuite.sourceforge.net). The healthy volunteer indicated epochs of voluntary eye closure using a switch synchronized to the EEG recording.

EEG signals were notch-filtered (55 to 65 Hz) before further processing, and epochs of eye closure were identified using the synchronized digital signal. Spectrograms were generated using wavelet transformation (Gabor). Cross-frequency coupling was computed using a Gabor wavelet and Gaussian window convolution with duration matched to frequency to generate a comodulogram. Correlation matrix was calculated using the magnitude of the wavelet components. $P < 0.05$ was considered statistically significant after Bonferroni-Holm correction for multiple comparisons.

SUPPLEMENTARY MATERIALS

Supplementary material for this article is available at http://advances.sciencemag.org/cgi/content/full/5/2/eaau7378/DC1

Fig. S1. Fabrication process and IGT architecture.
Fig. S2. PEDOT:PSS reduces the chitosan-Au electrochemical impedance at the IGT gate.
Fig. S3. Comparison of electrochemical impedance of different material interfaces.
Fig. S4. Comparison of ion species and ion membrane material on modulation magnitude and rise time of IGTs.
Fig. S5. Internal mobile ions enable stable operation over time without a decrement in speed or significant drift in drain current.
Fig. S6. Effect of channel geometry on IGT I_{on}/I_{off}.
Fig. S7. Output characteristics of IGT and OECT devices with identical geometry.
Fig. S8. Output characteristics of IGT and SS-OECT devices with identical geometry.

REFERENCES AND NOTES

1. K. Deisseroth, Optogenetics: 10 years of microbial opsins in neuroscience. *Nat. Neurosci.* **18**, 1213–1225 (2015).
2. M. Vöröslakos, Y. Takeuchi, K. Brinyiczki, T. Zombori, A. Oliva, A. Fernández-Ruiz, G. Kozák, Z. T. Kincses, B. Iványi, G. Buzsáki, A. Berényi, Direct effects of transcranial electric stimulation on brain circuits in rats and humans. *Nat. Commun.* **9**, 483 (2018).
3. E. Krook-Magnuson, J. N. Gelinas, I. Soltesz, G. Buzsáki, Neuroelectronics and biooptics: Closed-loop technologies in neurological disorders. *JAMA Neurol.* **72**, 823–829 (2015).
4. M. Voelker, P. Fromherz, Signal transmission from individual mammalian nerve cell to field-effect transistor. *Small* **1**, 206–210 (2005).
5. J. J. Jun, N. A. Steinmetz, J. H. Siegle, D. J. Denman, M. Bauza, B. Barbarits, A. K. Lee, C. A. Anastassiou, A. Andrei, Ç. Aydin, M. Barbic, T. J. Blanche, V. Bonin, J. Couto, B. Dutta, S. L. Gratiy, D. A. Gutnisky, M. Häusser, B. Karsh, P. Ledochowitsch, C. M. Lopez, C. Mitelut, S. Musa, M. Okun, M. Pachitariu, J. Putzeys, P. D. Rich, C. Rossant, W.-l. Sun, K. Svoboda, M. Carandini, K. D. Harris, C. Koch, J. O'Keefe, T. D. Harris, Fully integrated silicon probes for high-density recording of neural activity. *Nature* **551**, 232–236 (2017).
6. D.-H. Kim, J.-H. Ahn, W. M. Choi, H.-S. Kim, T.-H. Kim, J. Song, Y. Y. Huang, Z. Liu, C. Lu, J. A. Rogers, Stretchable and foldable silicon integrated circuits. *Science* **320**, 507–511 (2008).
7. J. A. Rogers, T. Someya, Y. Huang, Materials and mechanics for stretchable electronics. *Science* **327**, 1603–1607 (2010).
8. A. Tsumura, H. Koezuka, T. Ando, Macromolecular electronic device: Field-effect transistor with a polythiophene thin film. *Appl. Phys. Lett.* **49**, 1210–1212 (1986).
9. C. D. Dimitrakopoulos, P. R. L. Malenfant, Organic thin film transistors for large area electronics. *Adv. Mater.* **14**, 99–117 (2002).
10. T. Someya, T. Sekitani, S. Iba, Y. Kato, H. Kawaguchi, T. Sakurai, A large-area, flexible pressure sensor matrix with organic field-effect transistors for artificial skin applications. *Proc. Natl. Acad. Sci. U.S.A.* **101**, 9966–9970 (2004).
11. B. Crone, A. Dodabalapur, Y.-Y. Lin, R. W. Filas, Z. Bao, A. LaDuca, R. Sarpeshkar, H. E. Katz, W. Li, Large-scale complementary integrated circuits based on organic transistors. *Nature* **403**, 521–523 (2000).
12. H. Fang, J. Zhao, K. J. Yu, E. Song, A. B. Farimani, C.-H. Chiang, X. Jin, Y. Xue, D. Xu, W. Du, K. J. Seo, Y. Zhong, Z. Yang, S. M. Won, G. Fang, S. W. Choi, S. Chaudhuri, Y. Huang, M. A. Alam, J. Viventi, N. R. Aluru, J. A. Rogers, Ultrathin, transferred layers of thermally grown silicon dioxide as biofluid barriers for biointegrated flexible electronic systems. *Proc. Natl. Acad. Sci. U.S.A.* **113**, 11682–11687 (2016).
13. M. J. Panzer, C. R. Newman, C. D. Frisbie, Low-voltage operation of a pentacene field-effect transistor with a polymer electrolyte gate dielectric. *Appl. Phys. Lett.* **86**, 103503 (2005).
14. H. Shimotani, H. Asanuma, J. Takeya, Y. Iwasa, Electrolyte-gated charge accumulation in organic single crystals. *Appl. Phys. Lett.* **89**, 203501 (2006).
15. S. Ono, K. Miwa, S. Seki, J. Takeya, A comparative study of organic single-crystal transistors gated with various ionic-liquid electrolytes. *Appl. Phys. Lett.* **94**, 063301 (2009).
16. J. H. Cho, J. Lee, Y. He, B. S. Kim, T. P. Lodge, C. D. Frisbie, High-capacitance ion gel gate dielectrics with faster polarization response times for organic thin film transistors. *Adv. Mater.* **20**, 686–690 (2008).
17. A. Facchetti, Gels excel. *Nat. Mater.* **7**, 839–840 (2008).
18. E. Said, O. Larsson, M. Berggren, X. Crispin, Effects of the ionic currents in electrolyte-gated organic field-effect transistors. *Adv. Funct. Mater.* **18**, 3529–3536 (2008).
19. M. Hamedi, L. Herlogsson, X. Crispin, R. Marcilla, M. Berggren, O. Inganäs, Fiber-embedded electrolyte-gated field-effect transistors for e-Textiles. *Adv. Mater.* **21**, 573–577 (2009).
20. O. Knopfmacher, M. L. Hammock, A. L. Appleton, G. Schwartz, J. Mei, T. Lei, J. Pei, Z. Bao, Highly stable organic polymer field-effect transistor sensor for selective detection in the marine environment. *Nat. Commun.* **5**, 2954 (2014).
21. M. Ha, Y. Xia, A. A. Green, W. Zhang, M. J. Renn, C. H. Kim, M. C. Hersam, C. D. Frisbie, Printed, sub-3V digital circuits on plastic from aqueous carbon nanotube inks. *ACS Nano* **4**, 4388–4395 (2010).
22. H. S. White, G. P. Kittlesen, M. S. Wrighton, Chemical derivatization of an array of three gold microelectrodes with polypyrrole: Fabrication of a molecule-based transistor. *J. Am. Chem. Soc.* **106**, 5375–5377 (1984).
23. J. Rivnay, S. Inal, A. Salleo, R. M. Owens, M. Berggren, G. G. Malliaras, Organic electrochemical transistors. *Nat. Rev. Mater.* **3**, 17086 (2018).
24. D. Khodagholy, J. Rivnay, M. Sessolo, M. Gurfinkel, P. Leleux, L. H. Jimison, E. Stavrinidou, T. Herve, S. Sanaur, R. M. Owens, G. G. Malliaras, High transconductance organic electrochemical transistors. *Nat. Commun.* **4**, 2133 (2013).
25. E. Stavrinidou, R. Gabrielsson, E. Gomez, X. Crispin, O. Nilsson, D. T. Simon, M. Berggren, Electronic plants. *Sci. Adv.* **1**, e1501136 (2015).
26. L. H. Jimison, S. A. Tria, D. Khodagholy, M. Gurfinkel, E. Lanzarini, A. Hama, G. G. Malliaras, R. M. Owens, Measurement of barrier tissue integrity with an organic electrochemical transistor. *Adv. Mater.* **24**, 5919–5923 (2012).
27. S. Y. Yang, J. A. DeFranco, Y. A. Sylvester, T. J. Gobert, D. J. Macaya, R. M. Owens, G. G. Malliaras, Integration of a surface-directed microfluidic system with an organic electrochemical transistor array for multi-analyte biosensors. *Lab Chip* **9**, 704–708 (2009).
28. M. H. Bolin, K. Svennersten, D. Nilsson, A. Sawatdee, E. W. H. Jager, A. Richter-Dahlfors, M. Berggren, Active control of epithelial cell-density gradients grown along the channel of an organic electrochemical transistor. *Adv. Mater.* **21**, 4379–4382 (2009).
29. D. Khodagholy, T. Doublet, P. Quilichini, M. Gurfinkel, P. Leleux, A. Ghestem, E. Ismailova, T. Hervé, S. Sanaur, C. Bernard, G. G. Malliaras, In vivo recordings of brain activity using organic transistors. *Nat. Commun.* **4**, 1575 (2013).
30. P. Gkoupidenis, D. A. Koutsouras, G. G. Malliaras, Neuromorphic device architectures with global connectivity through electrolyte gating. *Nat. Commun.* **8**, 15448 (2017).
31. Y. van De Burgt, E. Lubberman, E. J. Fuller, S. T. Keene, G. C. Faria, S. Agarwal, M. J. Marinella, A. Alec Talin, A. Salleo, A non-volatile organic electrochemical device as a low-voltage artificial synapse for neuromorphic computing. *Nat. Mater.* **16**, 414–418 (2017).
32. D. A. Bernards, G. G. Malliaras, Steady-state and transient behavior of organic electrochemical transistors. *Adv. Funct. Mater.* **17**, 3538–3544 (2007).
33. D. Khodagholy, M. Gurfinkel, E. Stavrinidou, P. Leleux, T. Herve, S. Sanaur, G. G. Malliaras, High speed and high density organic electrochemical transistor arrays. *Appl. Phys. Lett.* **99**, 163304 (2011).
34. A. M. Nardes, R. A. J. Janssen, M. Kemerink, A morphological model for the solvent-enhanced conductivity of PEDOT:PSS thin films. *Adv. Funct. Mater.* **18**, 865–871 (2008).
35. J. Rivnay, S. Inal, B. A. Collins, M. Sessolo, E. Stavrinidou, X. Strakosas, C. Tassone, D. M. Delongchamp, G. G. Malliaras, Structural control of mixed ionic and electronic transport in conducting polymers. *Nat. Commun.* **7**, 11287 (2016).
36. G. D. Spyropoulos, C. O. Ramirez Quiroz, M. Salvador, Y. Hou, N. Gasparini, P. Schweizer, J. Adams, P. Kubis, N. Li, E. Spiecker, T. Ameri, H. J. Egelhaaf, C. J. Brabec, Organic and perovskite solar modules innovated by adhesive top electrode and depth-resolved laser patterning. *Energy Environ. Sci.* **9**, 2302–2313 (2016).

37. J. C. Cheng, T. H. Cauley, A. P. Pisano, Lithographic patterning of immobilized enzymes in chitosan thin films for multi-layer, chemical/biological sensors, 2007 7th IEEE Conference on Nanotechnol (IEEE-NANO 2007), pp. 334–337.
38. M. N. V. Ravi Kumar, A review of chitin and chitosan applications. *React. Funct. Polym.* **46**, 1–27 (2000).
39. M. Sheliakina, A. B. Mostert, P. Meredith, An all-solid-state biocompatible ion-to-electron transducer for bioelectronics. *Mater. Horiz.* **5**, 256–263 (2018).
40. K. Tybrandt, R. Forchheimer, M. Berggren, Logic gates based on ion transistors. *Nat. Commun.* **3**, 871–876 (2012).
41. M. Berggren, D. Nilsson, N. D. Robinson, Organic materials for printed electronics. *Nat. Mater.* **6**, 3–5 (2007).
42. W. Takashima, K. Sasano, T. Asano, K. Kaneto, Electroplasticity memory devices using conducting polymers and solid polymer electrolytes. *Polym. Int.* **27**, 249–253 (1992).
43. P. A. Ersman, D. Westerberg, D. Tu, M. Nilsson, J. Åhlin, A. Eveborn, A. Lagerlöf, D. Nilsson, M. Sandberg, P. Norberg, M. Berggren, R. Forchheimer, G. Gustafsson, Screen printed digital circuits based on vertical organic electrochemical transistors. *Flex. Print. Electron.* **2**, 045008 (2017).
44. E. S. Kappenman, S. J. Luck, The effects of electrode impedance on data quality and statistical significance in ERP recordings. *Psychophysiology* **47**, 888–904 (2010).
45. R. T. Canolty, E. Edwards, S. S. Dalal, M. Soltani, S. S. Nagarajan, H. E. Kirsch, M. S. Berger, N. M. Barbaro, R. T. Knight, High gamma power is phase-locked to theta oscillations in human neocortex. *Science* **313**, 1626–1628 (2006).
46. D. Khodagholy, J. N. Gelinas, G. Buzsáki, Learning-enhanced coupling between ripple oscillations in association cortices and hippocampus. *Science* **358**, 369–372 (2017).

Acknowledgments

Funding: This work was supported by Columbia University School of Engineering and Applied Science and Columbia University Medical Center Department of Neurology and Institute for Genomic Medicine. The device fabrication was performed at (i) Columbia Nano Initiative (CNI) and (ii) Cornell NanoScale Facility (CNF), a member of the National Nanotechnology Coordinated Infrastructure (NNCI), which is supported by the National Science Foundation (grant ECCS-1542081). G.D.S. is supported through the Human Frontiers Postdoctoral Fellowship Program. We thank E. Stavrinidou (University of Linkoping) and G. Malliaras (Cambridge University), I. Kymissis (Columbia University), M. Gonzalez, J. Yu, J. Vichiconti, N. Porecki-Shamay, N. Ariel-Sternberg (CNI), and all Khodagholy and Gelinas laboratory members for their support. **Author contributions:** D.K., J.N.G., and G.D.S. conceived the project, did the electrophysiology in vivo experiments and analysis, and wrote the paper. D.K. and G.D.S. designed, developed, fabricated, and characterized the devices. **Competing interests:** The authors declare that they have no competing interests. **Data and materials availability:** All data needed to evaluate the conclusions in the paper are present in the paper and/or the Supplementary Materials. Additional data related to this paper may be requested from the authors.

Submitted 10 July 2018
Accepted 9 January 2019
Published 27 February 2019
10.1126/sciadv.aau7378

Citation: G. D. Spyropoulos, J. N. Gelinas, D. Khodagholy, Internal ion-gated organic electrochemical transistor: A building block for integrated bioelectronics. *Sci. Adv.* **5**, eaau7378 (2019).

Internal ion-gated organic electrochemical transistor: A building block for integrated bioelectronics

George D. Spyropoulos, Jennifer N. Gelinas and Dion Khodagholy

Sci Adv **5** (2), eaau7378.
DOI: 10.1126/sciadv.aau7378